# Theoretical Investigation of Hyperthermal Reactions at the Gas−Liquid Interface: O ($^3$P) and Squalane

**Dongwook Kim and George C. Schatz***

*Department of Chemistry, Northwestern University, 2145 Sheridan Road, Evanston, Illinois 60208-3113.*

*Received: January 3, 2007; In Final Form: April 6, 2007*

Hyperthermal collisions (5 eV) of ground-state atomic oxygen [O ($^3$P)] with a liquid-saturated hydrocarbon, squalane ($C_{30}H_{62}$), have been studied using QM/MM hybrid "on-the-fly" direct dynamics. The surface structure of the liquid squalane is obtained from a classical molecular dynamics simulation using the OPLS-AA force field. The MSINDO semiempirical Hamiltonian is combined with OPLS-AA for the QM/MM calculations. In order to achieve a more consistent and efficient simulation of the collisions, we implemented a dynamic partitioning of the QM and MM atoms in which atoms are assigned to QM or MM regions based on their proximity to "seed" (open-shell) atoms that determine where bond making/breaking can occur. In addition, the number of seed atoms is allowed to increase or decrease as time evolves so that multiple reactive events can be described. The results show that H abstraction is the most important process for all incident angles, with H elimination, double H abstraction, and C−C bond cleavage also being important. A number of properties of these reactive channels, as well as inelastic nonreactive scattering, are investigated, including angular and translational energy distributions, the effect of incident collision angle, variation with depth of the reactive event within the liquid, with the reaction site on the hydrocarbon, and the effect of dynamics before and after reaction (direct reaction versus trapping reaction−desorption).

## I. Introduction

Ground-state atomic oxygen [O ($^3$P)] is the most abundant species in low Earth orbit (LEO).[1] Since a spacecraft in LEO travels at ∼7.4 km/s,[2] the collision energy between an oxygen atom and the spacecraft surface is about 5 eV. This leads to the degradation of polymeric materials coated on the vehicles;[3,4] therefore, there has been much interest in developing materials that are resistant to this degradation. Since space-based studies are difficult and expensive, there has been interest in alternatives, including the use of theoretical simulations, to study these problems. In addition, the theoretical methods can be used for studying polymer degradation more generally and thus are relevant to studies of cracking, embrittlement, delamination, discoloration, and other processes that are important in daily life.

The reaction of oxygen with saturated hydrocarbon polymers is one of the simplest examples of a polymer degradation process. It also is closely connected with reactions that are well-known in combustion and atmospheric chemistry. However, in the hyperthermal energy regime, there are many more open reactive channels than in combustion or atmospheric reactions, and many of these reaction mechanisms are not familiar from earth-based studies. Furthermore, even the characteristics of low-energy barrier processes can be significantly altered by hyperthermal conditions. In the past few years, several studies (both experiment and theory) of hyperthermal reactions between atomic oxygen and gaseous species[5−8] and between oxygen and surfaces[9−12] have been carried out. These studies have been enabled by recent advances in both experimental techniques and computational capabilities,[13,14] and for gas-phase processes, a detailed picture of the dominant reaction mechanisms has appeared. However, for gas−surface collisions, there are still important gaps in our understanding of the dynamical processes.

Understanding the dynamics of reactions between gaseous species and polymeric condensed phases has many areas of application, including chemical etching, adhesion, and biocompatibility enhancement, and this has stimulated a number of reaction dynamics studies in the past few years involving collisions of atoms with polymeric liquid surfaces.[15] Among these, because of its low vapor pressure, squalane is particularly important. Nathanson et al. employed squalane for their molecular beam studies of noble gas collisions in which two limiting processes, for example, direct inelastic collision and thermal trapping−desorption, were observed.[16] Related experiments were performed by Minton and co-workers involving a molecular beam of hyperthermal oxygen.[9−11] These measurements observed the production of O, OH, and $H_2O$ coming off in the gas phase, and it was proposed that inelastic collision and H abstraction proceed predominantly by a nonthermal Eley−Rideal pathway. In recent experiments,[11] C−C bond cleavage, the evaporation of intact squalane, and the abstraction of H by molecular $O_2$ was observed under hyperthermal conditions. For lower energy oxygen collisions, the McKendrick group performed laser-induced fluorescence (LIF) studies to determine the rovibrational states of the OH radical,[17,18] and they found that, although the products were rotationally quite cold, there was nonnegligible vibration excitation. These results were in good agreement with theoretical studies of oxygen reacting with an alkanethiol self-assembled monolayer (SAM) surface,[12,19] where it was found that the branching ratio ($\nu' = 1$)/($\nu' = 0$) was as large as 10%. They attributed the detected vibrationally hot OH radical to H abstraction from secondary and tertiary carbons on the squalane. To support this proposition, McKendrick conducted a complementary classical molecular dynamics (MD) simulation to determine the surface structure

* To whom correspondence should be addressed. E-mail: schatz@chem.northwestern.edu.

10.1021/jp0700478 CCC: $37.00 
Published on Web 05/19/2007

**TABLE 1: Comparison of Predicted Reaction Energies and Barriers for Representative Product Channels of the O + Methane and O + Ethane Reactions Using MSINDO and CCSD(T)[a,6,7]**

| | reaction energy | | reaction barrier | |
|---|---|---|---|---|
| | MSINDO | CCSD(T)[b] | MSINDO | CCSD(T)[b] |
| | | O + Methane | | |
| H abstraction | −0.342(−0.151) | 0.152(0.288) | 0.564(0.699) | 0.497(0.635) |
| H elimination | 0.081(0.284) | 0.778(0.950) | 1.869(1.986) | 2.096(2.204) |
| | | O + Ethane | | |
| H abstraction | −0.758(−0.589) | 0.042(0.223) | 0.370(0.513) | 0.415(0.571) |
| H elimination | −0.209(−0.007) | 0.608(0.827) | 1.701(1.879) | 2.191(2.330) |
| | | | 1.671(1.792) | 2.457(2.612) |
| C−C breakage | −0.720(−0.516) | 0.132(0.344) | 1.645(1.693) | 2.062(2.136) |

[a] All of the values are in eV, and the values in parentheses are evaluated without zero-point energy correction. [b] For the O + methane reaction, the CCSD(T) values are evaluated from the CCSD(T)/aug-cc-pVTZ single-point calculation at UMP2/aug-cc-pVDZ-optimized geometries and frequencies, and for the O + ethane reaction, they are from the CCSD(T)/cc-pVTZ single-point calculation at UMP2/cc-pVTZ-optimized geometries and frequencies. See refs 6 and 7.

of squalane and a Monte Carlo (MC) tracking simulation to estimate the accessibility of each type of carbon atom to O attack.[20] These results, which did not actually simulate reactive collisions, suggested that secondary carbons are as accessible as primary carbons to the incoming O atom. They also found that the recoiled products are likely to undergo secondary collisions.

Despite this earlier theoretical work related to the reaction of atomic oxygen with hydrocarbon surfaces,[12,19,21] the simulation of reactive collisions with squalane has not been previously reported. In this paper, we report such a study, with emphasis on characterizing the dynamics of the inelastic scattering, H abstraction, H elimination, and C−C bond breakage processes. In addition, we investigate the accessibility of the incoming O to each type of carbon in squalane. Our calculations use a novel quantum mechanics/molecular mechanics (QM/MM) approach to determine forces for molecular dynamics calculations in which the partitioning of atoms treated by quantum mechanics and by molecular mechanics is allowed to vary as the collision proceeds. This allows us to describe reactions in which there are several bond breaking/forming events and where there is significant restructuring of the liquid such that a partitioning based on the initial locations of the atoms (as is usually done) is not effective. Details of the QM/MM calculations are given in section 2, while the results and discussion are in section 3, and the conclusion is in section 4.

## II. Theoretical Methods

**A. Structure of the Squalane Surface.** Prior to the QM/MM calculations, we need to determine the surface structure of liquid squalane for a temperature and density that is relevant to the experiments. Although there have been several theoretical studies[20,22−26] of squalane including studies of the liquid surface structure,[20,26] all of them have been carried out utilizing a united atom model where the $-CH_3$, $-CH_2$, and $-CH$ fragments in squalane are treated as a single particle. However, since the reactions of interest in our study involve C−H bond cleavage, C−C bond breakage, and other processes, it is essential to include all atoms in our description. Therefore, we need to find an appropriate all-atom model force field for the simulation of squalane.

Two widely used empirical force fields have been considered, MM3[27] and OPLS-AA,[28] both within the TINKER package of programs.[29] As a preliminary step, we ran isobaric−isothermal (NPT) ensemble simulations for a homogeneous liquid of 48 squalane molecules with periodic boundary conditions (PBCs) in three dimensions. The simulation was run for 1.2 ns at 400 K and for 0.6 ns more at 298 K for the equilibration and data accumulation to determine the density. The pressure was maintained at 1 atm throughout the simulation. The bulk density of squalane for each force field was compared with the experimentally observed value, 0.815 g/cm$^3$, and it turns out that the OPLS-AA force field gives a better result (0.796 g/cm$^3$) than MM3 (0.696 g/cm$^3$). Therefore, we decided to use the OPLS-AA force field for the surface structure of squalane in subsequent simulations.

To simulate the liquid interface, the last configuration of the homogeneous liquid simulation was selected, and the box size was adjusted on the basis of the density obtained ($39.3 \times 39.3 \times 27.7$ Å$^3$). This structure was then used to define a slab of liquid by adding empty regions above and below the slab such that the total simulation box was elongated by a factor of 3 in one direction ($39.3 \times 39.3 \times 83.1$ Å$^3$). As a result, the squalane molecules at the top and bottom surfaces of the liquid did not interact when PBCs were applied; therefore, we can mimic a realistic gas−liquid interfacial structure. An NVT ensemble simulation was then performed at 400 K for 0.6 ns and then continued for 2 ns at 298 K for equilibration and data accumulation.

**B. Dynamics Calculations.** To investigate the dynamics of hyperthermal O ($^3$P) atoms colliding with squalane, molecular dynamics calculations are performed in which a portion of the atoms are treated by direct dynamics (DD) quantum mechanics (electronic structure) calculations and another portion are treated with empirical molecular mechanics potentials. There are several ways to define the interface between the reactive QM part and nonreactive MM part. Since our system is electrically neutral and charge transfer or interactions between the charges of the atoms can be assumed to be negligible, a simple mechanical embedding approach[30] should be reasonable.

For the QM calculations, we used the MSINDO (modified symmetrically orthogonalized intermediate neglect of differential overlap) semiempirical Hamiltonian.[31] A key reason for this choice is that MSINDO has been successful in predicting reaction energies and barriers for gas-phase reactions between O ($^3$P) and short hydrocarbons.[5−7] However, since we deal with reactions involving a liquid hydrocarbon, where there are a larger number of reaction energies and barriers than there were studied for the gas-phase reactions, it is useful to review both the advantages and disadvantages of the MSINDO method. Table 1 compares reaction energies and barriers for the O ($^3$P) + methane[7] and ethane reactions[6] as obtained from MSINDO and CCSD(T) calculations. The table shows that the agreement of the reaction barriers from both methods is remarkable. Since

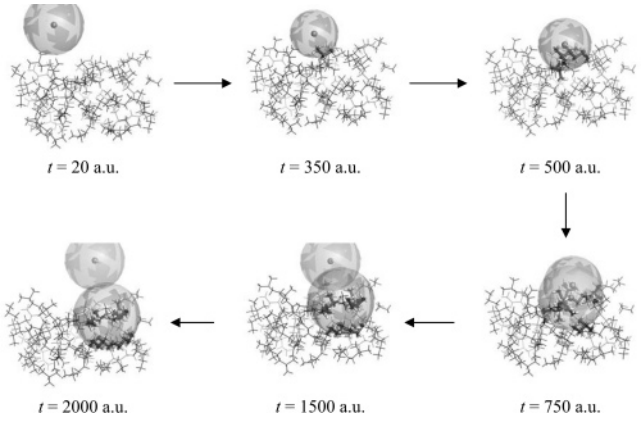


**Figure 1.** Illustration of the modified direct dynamics method. The spheres indicate the QM region around the QM seed atoms. As the incoming O approaches the surface, the QM sphere gradually includes a portion of the surface atoms. After that, the C atom whose H is abstracted by the O becomes a new seed atom. Later, the OH exits from the surface, releasing the QM atoms around it to the MM regime.

reactivity is typically determined by barrier height, we expect that this aspect of the reaction dynamics should be accurately determined from the MSINDO calculations. However, the table also shows that MSINDO systematically overestimates the reaction exoergicities compared to those from CCSD(T). This could lead to incorrect evaluation of the product energy disposal behavior (for gaseous products). This point will be examined later in the paper.

The fact that squalane is a liquid raises a concern that the incident O atom is likely to penetrate the surface easily, interacting with a large number of atoms both before and after reaction. Recent simulations of the O ($^3$P) + SAM[21] system indicate that it is possible for the O atom to be trapped for even ~60 ps, enabling transfer from one channel formed by the alkanethiol chains to another. In fact, we find that some gaseous species cannot be confined to a squalane slab that has a radius of 18 Å and a height of 20 Å, even though this contains approximately 2000 atoms. In addition, in contrast to O + SAM collisions where the alkanethiol chains are aligned periodically such that the QM region is spatially distinct, liquid squalane is amorphous and the molecules diffuse. Thus, a QM/MM partitioning based on fixed atoms will require a large QM part and thus large computational costs to produce reliable results.

To deal with this, we modified the conventional QM/MM method to allow atoms to be moved back and forth between QM and MM regions while the trajectory is being integrated. The standard link atom method[30] is used at the QM/MM boundary for atoms that are in the QM region. To identify the QM atoms, we assume that QM atoms are within the boundary of a sphere whose center is located at a seed atom. The seed atom is typically open-shell so that it serves as a site where reaction can occur. We also allow for the possibility that there might be several spheres and several seed atoms whose number might change with time. The radii of the spheres are chosen to be large enough so that all bond breakage and formation takes place within the spheres, while atoms moving between QM and MM regions are close to minimum energy structures where the QM and MM force fields are similar. In addition, we want to make the QM spheres as small as possible to reduce computational effort. Figure 1 shows how this works for a trajectory that leads to H abstraction. Here, the initial seed atom is taken to be the O atom. As the atom approaches the surface, some of the surface atoms move within the QM sphere such that the reactive event involves breaking and making bonds only between atoms in the QM region. When reaction occurs, the C atom which loses one of its H atoms is chosen to be a new seed atom since this atom is now open-shell and can serve as a site for further reaction. The O atom is also retained as a seed atom, as the OH radical is also open-shell and can undergo further reactions. However when the OH leaves the surface, atoms that are inside of the associated sphere will move outside of this sphere, and the atoms will change from being QM to MM.

One issue associated with this procedure is that when an atom is moved between QM and MM regions, there will be a discontinuity in the force for atoms near that atom. This effect could, in principle, lead to nonphysical behavior; however, we find that as long as the radius is chosen to be large enough, the effects are not significant. To determine this radius, we require that the force between C, O, and H atoms and methane located at the boundary of the sphere be smaller than $1 \times 10^{-7}$ hartree/bohr. This leads to radii of 10, 12.0, and 12.5 bohr for O, H, and C, respectively, and we have used these values for all further calculations. Obviously, the success of this procedure depends on the ability of the QM and MM forces to be similar in value for geometries where the atoms get relabeled. These geometries are far away from the reactive region, and so, the MM and QM potentials should be similar; however, some discontinuity in force is unavoidable.

There have been concerns in past work about the effects of discontinuities in the potential energy and forces in dynamic partitioning schemes such as those that we have developed, and several sophisticated algorithms have been devised to remove these discontinuities.[32−34] A recent study showed that to remove all discontinuities in potential energy and force, trajectories should be integrated with O($N$) or O($2^N$) multilevel calculations at each time step, depending upon the algorithm, whenever there are $N$ atoms or groups of atoms in the buffer between the QM and MM regions.[34] In the simulation of a system consisting of 171 argon atoms, for example, the average number of argon atoms in the buffer zone was 2.4; therefore, 3.3 or 8.8 multilevel calculations were needed in each time step. In liquid squalane, we have more carbon atoms (~4.4) at the QM/MM junction, and in the case where reaction occurs, the number of QM spheres linearly increases as a function of the number of broken bonds such that the application of one of the refined algorithms is computationally prohibitive. We also note that the past work[34] has demonstrated that the results from using the discontinuous method do not severely deviate from those of more sophisticated algorithms and, in fact, behave even better than the so-called "hot spot" method[32] in which the force (but not the potential) on the atoms in the buffer is smoothed.

To test the importance of discontinuities in the force, we have compared trajectories in which the partitioning between QM and MM atoms is not allowed to change with those where it is, looking specifically at inelastic collisions where the initial and final partitionings are same. We find that the variable partitioning trajectory shows energy conservation behavior that is comparable to that of fixed partitioning trajectories.

In a previous study,[35] the influence of excited states and triplet−singlet intersystem crossing on the excitation function of the hyperthermal O ($^3$P) + methane reaction was discussed. It was found that intersystem crossing has a negligible effect on the excitation function. However, the first excited triplet state contributes substantially to the cross section at energies well above the reactive threshold. Including the triplet excited states is prohibitive in the present simulation; therefore, the overall reactivity is expected to be underestimated. However, the

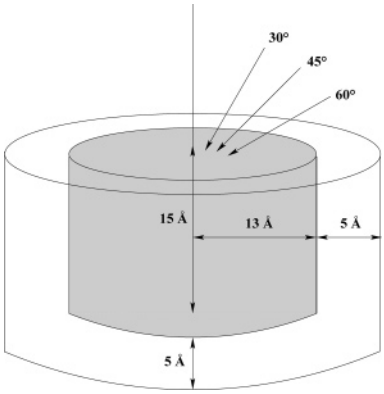


**Figure 2.** Schematic picture of the system. The core round box depicts the regime in which atoms move, and the peripheral shell region defines the atoms which are fixed. The arrows above the surface shows the incident angle, $\theta_i$.

qualitative aspects of the reaction dynamics are not expected to be different. Note that we have not factored in the electronic degeneracy factor of 1/3 in the reaction probabilities that we present.

The dynamics calculations are conducted by considering those squalanes in the slab defined above that are within a cylindrical region whose radius is 18 Å and height is 20 Å (Figure 2) to be mobile. Since we do not apply PBCs, we divide the cylinder into two regions, a peripheral buffer layer of 5 Å thickness and a core part. The fragments of squalane in the buffer are fixed, while those in the core region are allowed to move during the collision. The incident O ($^3$P) atom is launched with an initial translational energy of 5 eV and starting 15 au above the surface. The components of the velocity vectors of the O ($^3$P) atoms are determined by the angle ($\theta_i$) between the incident velocity vector and the surface normal and the azimuthal angle ($\phi$). We select five different squalane structures randomly from the previously described NVT simulation at room temperature (298 K) for our collision dynamics studies, and all of the results have been averaged over these structures. Results are generated for three incident angles, $\theta_i = 30$, 45, and 60°, and four azimuthal angles, $\phi = 0$, 90, 180, and 270°. In contrast to a SAM surface, the azimuthal angle has no relation to a specific structure of squalane. Thus, all results are averaged over the azimuthal angle. A total of 1400 trajectories have been generated by impacting the O at 25 different points on the surface from each of 12 different values of $\theta_i$ and $\phi$ for each squalane structure.

Trajectories are terminated if products from the reaction including inelastic scattering exit from the surface and reach 20 au above the surface. Trajectories are generally terminated at 3 ps duration if the products are confined in the squalane at that point. However, in cases where the products are close to being desorbed at 3 ps, the integration is continued until the product has escaped. This usually takes less than a total of 5−6 ps.

It should be noted that some hyperthermal oxygens penetrate so deeply that the 20 Å-thick squalane slab used in the present studies cannot prevent these atoms from completely penetrating the slab. Increasing the size of the squalane slab, however, entails more computational cost, which is prohibitive at the moment. Fortunately, these trajectories are of low probability.

## III. Results and Discussion

**A. Reaction Statistics.** Table 2 shows the reaction probabilities for different incident angles ($\theta_i = 30$, 45, and 60°) at a collision energy of 5 eV. This shows that H abstraction to give OH is the dominant reaction process regardless of the incident angle. Inelastic scattering, double H abstraction generating $H_2O$, and H elimination to produce an alkoxy radical are the three next most important processes. C−C bond cleavage is also observed, but this is a minor process. As found in the earlier study of O + SAM,[12] multiple reaction steps can occur in a single collision, including double H elimination, H elimination + C−C bond cleavage, and double C−C bond breakage. These can occur either concurrently or sequentially. The probabilities of these processes are included separately from the aforementioned reactions. In addition, although the cases are very rare and thus are categorized into "etc", secondary H abstraction by a species other than the O atom is also seen, for example, $H_2$ and $CH_4$ are produced through H abstraction by H and $CH_3$ radicals, respectively.

**TABLE 2: Probabilities of Inelastic and Reactive Process for the Hyperthermal Collision of O ($^3$P) with Liquid Squalane at 5 eV for Different Incident Angles $\theta_i$[a]**

| $\theta_i$ | 30° | 45° | 60° |
|---|---|---|---|
| inelastic collision | 0.20 (0.69) | 0.18 (0.83) | 0.31 (0.84) |
| H abstraction | 0.41 (0.71) | 0.41 (0.80) | 0.41 (0.83) |
| double H abstraction | 0.16 (0.76) | 0.22 (0.69) | 0.08 (0.80) |
| H elimination | 0.14 (0.95) | 0.12 (0.92) | 0.14 (0.96) |
| C−C bond cleavage | 0.06 (0.62) | 0.06 (0.71) | 0.06 (0.60) |
| etc[b] | 0.01 (1.00) | 0.00 (0.00) | 0.00 (1.00) |

[a] The values in parentheses represent the probability that the reaction product exits from the liquid surface and is in the gas phase. [b] The extra cases include combinations of the primary reaction mechanisms, for example, H abstraction by eliminated H or detached $CH_3$, resulting in $H_2$ and the $CH_4$ molecule, respectively.

While reactivity appears to be independent of the incident azimuthal angle, as mentioned in the previous section, the variation in reactivity with incident polar angle is important, as associating it with the geometric features of squalane at the surface provides a physical picture of the reaction dynamics. For example, the probability of H abstraction is independent of incident angle, although the trapping fraction after a 3 ps integration time depends on it. In addition, C−C bond scission is also independent of incident angle, but inelastic scattering varies with angle such that the highest probability is at $\theta_i = 60°$ and the smallest is for $\theta_i = 45°$. On the other hand, double H abstraction varies inversely to inelastic scattering, that is, it happens the most at 45° and the least at 60°. In the case of H elimination, $\theta_i = 30$ and 60° show similar probabilities, with a slightly lower probability at 45°.

These trends in reactivity with incident angle are quite different from what was observed in the O + SAM studies,[12] where it was found that reactivity was strongly dependent on geometry, as determined by the cone of acceptance of the incident oxygen atom at the point of impact at the first carbon atom encountered. This dependence was tied to the fixed orientation of the SAM molecules relative to the gold substrate of the SAM; therefore, it is perhaps not surprising that these trends are not found for squalane. However, incident impact geometry is still important in the squalane case. For example, most H elimination reactions occur when the incoming O impinges directly on a carbon near the surface. Since the orientation of bonds around this carbon is largely random for squalane, this explains why the reaction probability is not sensitive to the incident approach direction. Another issue that plays a role in collisions with squalane is the mean residence time, $<\tau>$, during which the projectile travels under the surface. This time and the probability of not penetrating the surface to the point where the density is half of its bulk value, $P(\tau = 0)$, for inelastic collisions and H abstraction are listed in Table 3.

**TABLE 3: The Mean Residence Time, $<\tau>$, and the Probability of $\tau = 0$ for Inelastic Scattering and H Abstraction[a]**

| $\theta_i$ | 30° | 45° | 60° |
|---|---|---|---|
| | Inelastic Collision | | |
| $<\tau>$ | 705 ± 106 | 276 ± 61 | 95 ± 39 |
| $P(\tau = 0)$ | 0.18 | 0.51 | 0.74 |
| | H Abstraction | | |
| $<\tau>$ | 571 ± 61 | 420 ± 49 | 205 ± 40 |
| $P(\tau = 0)$ | 0.20 | 0.34 | 0.61 |

[a] The $<\tau>$ is in femtosecond. $P(\tau = 0)$ represents the probability that the incoming O or the product OH scatters off the 50% density dividing surface without penetrating it.

For $\theta_i = 60°$, direct scattering off of the surface is important, and $<\tau>$ is the smallest. In the case of H abstraction, the product OH does not generally have sufficient time to encounter another object and abstract another H atom. Therefore, although the probability of H abstraction for $\theta_i = 60°$ is similar to that for the other incident angles, there is a much smaller probability of generating $H_2O$. In addition, the projectile experiences a smaller number of impacts for $\theta_i = 60°$, and thus, the likelihood of inelastic collision is high. On the other hand, for $\theta_i = 30°$, we see increased probability of double abstraction and a smaller probability of inelastic collision. Also, the O atom spends a longer time in the liquid; therefore, it is more likely to react and more likely to give a trapped product, and there is more energy transfer to the hydrocarbon. Thus for 30°, we find enhanced probabilities of trapping for inelastic collisions and H abstraction.

Similar to the previous studies,[21,36] we have also counted the number of encounters of the incoming O with liquid squalane to delve further into the mechanism of energy transfer (Figure 3). Encounters are counted when the maximum in the instantaneous force exerted on the projectile or on the product center-of-mass is larger than 0.5 eV/Å. It turns out that below this amount, the projectile or product hardly changes its trajectory, and hence, energy transfer is not important. A graph showing the final product translational energy $E_T$ versus the number of encounters, $N_{enc.}$ for inelastic collisions is presented in Figure 3. In this figure, significant energy transfer from the incoming O is observed for the first few encounters (for example, 1−5) for the smaller incident angle. As the incident angle increases, the distribution of transferred energy in the first few collisions becomes broader.

For $\theta_i = 45°$, the projectile spends more time under the surface than that for $\theta_i = 60°$, and therefore, it is more likely to undergo a reactive collision. On the other hand, when it escapes from the liquid, the newly formed OH projectile has lost less energy than that for $\theta_i = 30°$ such that the product has a smaller probability of being trapped and is more likely to experience secondary reaction. As a result, we see a smaller probability of inelastic collision and the highest likelihood of double H abstraction.

In case of C−C bond cleavage, no distinct variation with the initial conditions is observed. The reason seems similar to the case of H elimination. The reaction barriers between O and ethane for H elimination and C−C bond scission are similar (1.67−1.70 eV for H elimination and ∼1.65 eV for C−C bond scission) based on MSINDO.[6] Hence, it is more likely that C−C bond scission takes place in the first few impacts between the impinging O atom and squalane so that the O atom will have sufficient energy to overcome the barrier. Since there is no clear geometric ordering of squalane near the surface except the slight tendency of the methyl groups to point out toward vacuum,[20,26]

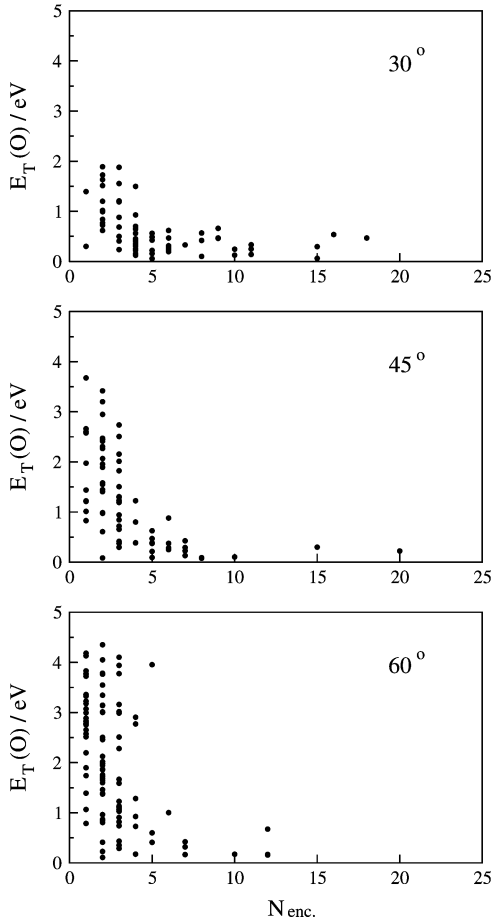


**Figure 3.** Scatter plots of $E_T$ versus $N_{enc.}$ for inelastic scattering at different incident angles.

variation in the C−C bond cleavage probability with incident angle is minor.

McKendrick and co-workers showed in their recent study that the accessibility of the incident O atom to each type of hydrogen is qualitatively in accord with relative abundance.[20] In their report, however, the relative reactivity of each type of C−H bond was not taken into account. In addition, they focused on the first impact in their model of H abstraction, even though they mentioned the possibility of H abstraction in secondary collisions. We consider the accessibility to each type of carbon rather than hydrogen because the spectrum of reactions (including H elimination, C−C bond breakage) is more closely connected with impacts on carbon atoms (including the possibility of a O−H−C− conformation at the transition state).

We mentioned that the surface structure of squalane is very disordered. However, statistically, there are distinct characteristics in terms of the distribution of each carbon segment with respect to distance beneath the surface.[20,26] Figure 4 shows the number density (beads/Å$^3$) of primary, secondary, and tertiary carbons at the squalane interface, with a vertical line denoting the position where the density is half of its bulk value (which can be thought of as the nominal interface location). In the bulk region, we see ratios of primary to secondary to tertiary carbons which match their expected statistical values (Pri./Sec./Tert. = 8:16:6). However, the abundance of primary C is similar to that of secondary C for locations at or above the vertical line, indicating that the methyl groups are preferentially located in the interfacial region. The accessibility of each type of carbon to reaction is listed in Table 4, and this indicates that when summed over all reactive channels, the fraction of reaction is

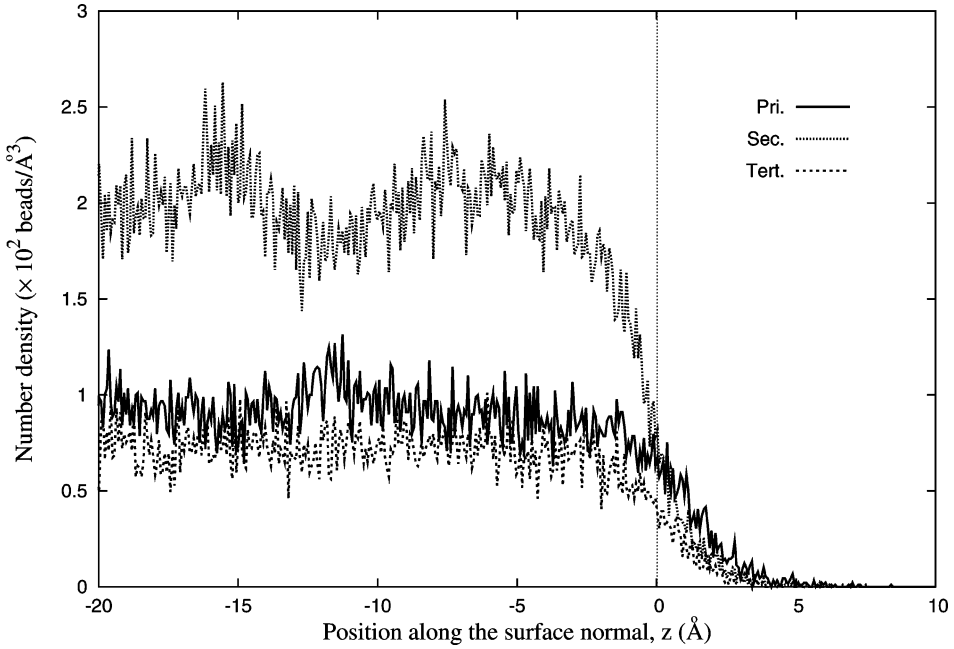


**Figure 4.** Segment number density profile for squalane as function of position (*z*) along the surface normal.

**TABLE 4: Reaction Probabilities at Primary, Secondary, and Tertiary Segments for the Hyperthermal Collision of O ($^3$P) with Liquid Squalane at 5 eV for Different Incident Angles $\theta$**

| | 30° | 45° | 60° | total |
|---|---|---|---|---|
| First H Abstraction[a] | | | | |
| primary | 0.18 | 0.24 | 0.26 | 0.23 |
| secondary | 0.56 | 0.49 | 0.49 | 0.51 |
| tertiary | 0.26 | 0.28 | 0.25 | 0.26 |
| Second H Abstraction[b] | | | | |
| primary | 0.17 | 0.21 | 0.22 | 0.20 |
| secondary | 0.53 | 0.51 | 0.47 | 0.51 |
| tertiary | 0.30 | 0.28 | 0.31 | 0.29 |
| Subtotal for H Abstraction | | | | |
| primary | 0.18 | 0.23 | 0.26 | 0.22 |
| secondary | 0.55 | 0.49 | 0.49 | 0.51 |
| tertiary | 0.27 | 0.28 | 0.26 | 0.27 |
| H Elimination | | | | |
| primary | 0.46 | 0.40 | 0.51 | 0.46 |
| secondary | 0.50 | 0.48 | 0.36 | 0.45 |
| tertiary | 0.04 | 0.12 | 0.13 | 0.09 |
| C−C Bond Cleavage | | | | |
| primary | 0.15 | 0.14 | 0.28 | 0.19 |
| secondary | 0.55 | 0.32 | 0.32 | 0.40 |
| tertiary | 0.30 | 0.54 | 0.40 | 0.41 |
| Subtotal for O Impact on C[c] | | | | |
| primary | 0.37 | 0.32 | 0.44 | 0.38 |
| secondary | 0.52 | 0.43 | 0.35 | 0.43 |
| tertiary | 0.11 | 0.15 | 0.21 | 0.19 |
| Total Statistics | | | | |
| primary | 0.23 | 0.25 | 0.31 | 0.26 |
| secondary | 0.54 | 0.48 | 0.44 | 0.49 |
| tertiary | 0.23 | 0.27 | 0.24 | 0.25 |

[a] The first H abstraction includes both single H abstraction and the first H abstraction of the double H abstraction. [b] The second H abstraction represents H abstraction by OH radical-generating $H_2O$. [c] Impact on C includes reactions which generate alkoxy radicals or ketones.

in fair agreement with the statistical values (0.27:0.53:0.20) for the carbon abundances. However, a slight preference for tertiary carbon is observed that will be discussed below. For H abstraction, the reaction probabilities are closer to the carbon statistical abundances than to the hydrogen statistical abundances (0.39:0.51:0.10). However, for H elimination, which is induced by bond formation between O and C, the probabilities are more in accord with the hydrogen abundances. This somewhat surprising result can be understood based on the fact (shown below) that H elimination tends to occur at the squalane surface where primary carbons are more abundant (Figure 4), while abstraction occurs more in the interior where bulk statistics are appropriate. Both of these reactive channels arise from the first few impacts where the oxygen still has high translational energy, and the barrier to reaction is less important.

**TABLE 5: The Average Position of the Incoming O at the Moment of Reaction with Respect to the Gibbs Dividing Surface, $\langle z_{rxn} \rangle$, in Terms of the Reaction Channel and Type of Counterpart Carbon Segment for Different Incident Angles[a]**

| $\theta_i$ | 30° | 45° | 60° |
|---|---|---|---|
| total | $-2.56 \pm 0.15$ | $-2.08 \pm 0.12$ | $-1.30 \pm 0.15$ |
| Reaction Type | | | |
| inelastic collision[b] | $-7.23 \pm 0.29$ | $-3.30 \pm 0.13$ | $-2.48 \pm 0.16$ |
| H abstraction | $-2.87 \pm 0.18$ | $-2.27 \pm 0.14$ | $-1.60 \pm 0.20$ |
| H elimination | $-1.23 \pm 0.27$ | $-0.97 \pm 0.23$ | $-0.50 \pm 0.17$ |
| C−C bond cleavage | $-2.65 \pm 0.37$ | $-2.16 \pm 0.42$ | $-0.89 \pm 0.20$ |
| Type of Carbon | | | |
| primary | $-0.76 \pm 0.27$ | $-0.54 \pm 0.19$ | $-0.07 \pm 0.20$ |
| secondary | $-3.39 \pm 0.20$ | $-2.65 \pm 0.17$ | $-1.73 \pm 0.25$ |
| tertiary | $-2.43 \pm 0.25$ | $-2.51 \pm 0.22$ | $-2.06 \pm 0.24$ |

[a] All of the values are in Å. [b] For inelastic collisions, $\langle z_{rxn} \rangle$ is defined as the deepest point of penetration of the projectile.

For C−C bond breakage, we see results that are more in accord with the number of C−C bonds for each type of carbon (0.14:0.55:0.31) than to the other statistical measures, especially for $\theta_i = 30°$ where the agreement is remarkable. Presumably, for $\theta_i = 30°$, the incoming O penetrates deeper during the first several impacts so that bulk statistics are more relevant.

To understand how penetration depth correlates with incident angle, in Table 5, we present the average position of the O atom (using the coordinate *z* defined in Figure 4) at the moment of reaction as a function of reaction type, carbon atom site, and

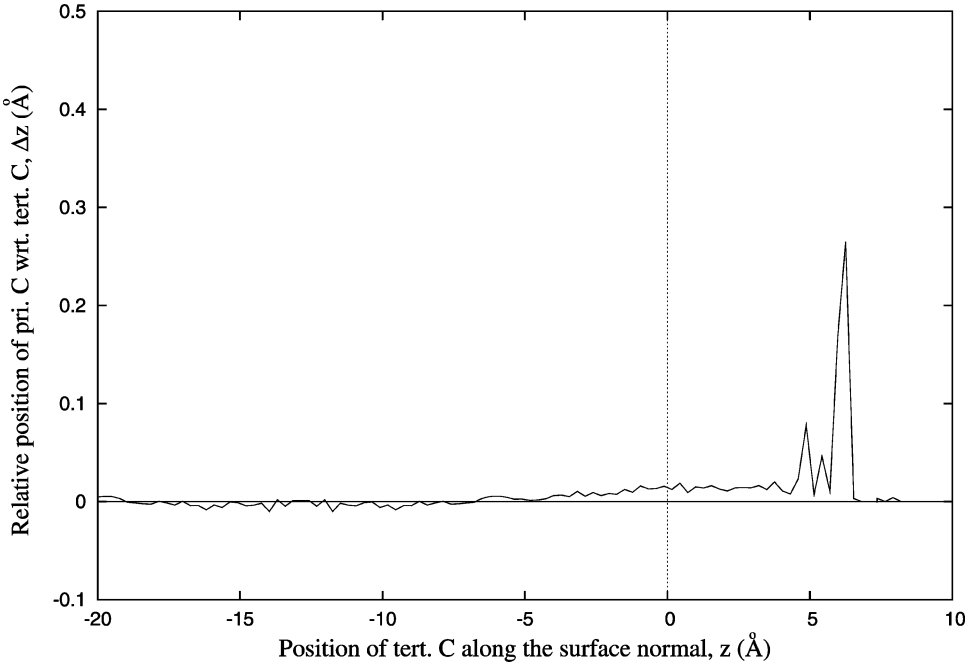


**Figure 5.** Relative position (along the surface normal), Δz, of the primary carbon with respect to its adjacent tertiary carbon as function of the location of the tertiary carbon. Positive values indicate that at the position of a given tertiary carbon, the adjacent-bound primary carbon is located above it (toward vacuum).

**TABLE 6: Average Translational Energy of the Incoming O at the Moment of H Abstraction[a]**

| $\theta_i$ | 30° | 45° | 60° | total |
|---|---|---|---|---|
| primary | 2.93 ± 0.38 | 2.80 ± 0.28 | 2.97 ± 0.32 | 2.89 ± 0.06 |
| secondary | 2.81 ± 0.10 | 2.52 ± 0.06 | 2.91 ± 0.11 | 2.73 ± 0.06 |
| tertiary | 2.15 ± 0.14 | 2.55 ± 0.07 | 1.95 ± 0.19 | 2.24 ± 0.10 |
| total | 2.65 ± 0.08 | 2.60 ± 0.06 | 2.70 ± 0.08 | |

[a] All of the values are in eV.

incident angle. This shows that, when averaged over reaction type, the average *z* values are −2.56, −2.08, and −1.30 Å for 30, 45, and 60°, respectively. The data also indicate that reaction with primary carbons take place closer to the surface, while those with secondary and tertiary carbons occur deeper under the surface. It is also apparent that since the incoming O atom reacts in the first several collisions and the incoming O atom is able to penetrate the surface into bulk more effectively prior to the reaction when the incident angle is close to the surface normal, secondary carbons are more accessible.

Interestingly, reaction with tertiary carbons occurs around 2 Å deeper on average than with primary carbons. This occurs despite the fact that the depth profile distributions of primary and tertiary carbons are very similar due to the fact that every primary carbon is attached to a tertiary carbon in squalane (Figure 4). To judge the significance of this 2 Å difference, we investigated the relative position of the primary carbon with respect to its adjacent tertiary carbon along the surface normal (Figure 5). In the outermost interfacial region, primary carbons tend to point out to the vacuum such that they are located above their binding tertiary carbons. However, this tendency disappears abruptly even at the nominal surface (vertical line in Figure 5), and finally, there is no position difference for tertiary carbons in the bulk. Furthermore, the maximum difference appears not to exceed 1 Å, and thus, the 2 Å difference, which may seem meaningless, has some significant implication. Apparently, steric hindrance prevents the O atom from approaching the tertiary carbon, and this leads to the difference in depth of reaction. Primary carbons are relatively open to O-atom attack, and therefore, the reaction probability with surface atoms is high. On the other hand, since the tertiary carbons are shielded by three adjacent carbons, the probability of reaction in the first impact is smaller, and reaction therefore occurs deeper into the surface. Another consequence is that the incoming O atom loses more of its energy before reaction occurs. Table 6 provides an inkling of this, showing that for all incident angles, in the case of H abstraction, the average kinetic energy of O at the moment of the reaction is higher for primary carbons than that for tertiary carbons.

For secondary carbons, Table 5 shows that the average reaction position moves deeper into the liquid as the incident angle decreases. This tendency is somewhat weakened for primary carbons, which presumably reflects their relative abundance in the interfacial region and their availability to collision. As for the reaction with tertiary carbons, the projectile typically undergoes multiple collisions before reaction at a tertiary site, and the barrier to reaction is lower; therefore, the dependence on incident angle is weak.

The average product translational energy, $<E_T>$, and final scattering angle, $<\theta_f>$, for several representative processes including experimental values[37] are presented in Table 7. Since the products have only been detected for forward azimuthal angles in the experiment,[10] average values for scattering in the forward direction are also provided for the comparison of theory and experiment. These theoretical results are in good agreement with experiment. For inelastic scattering and H abstraction, $<E_T>$ and $<\theta_f>$ decreases as the incident angle becomes closer to normal, and on the other hand, these quantities are largely independent of initial conditions for H elimination. These results will be discussed later. It is also worthwhile to note that including only the forward azimuthal angles tends to give higher $<E_T>$ and $<\theta_f>$ values, indicating that the products recoiling backward have less energy and exit closer to the surface normal than those recoiling forward.

In the following subsections, we examine more details of the dynamics for the most important reaction channels.

**B. Inelastic Scattering.** When hyperthermal O strikes the surface of liquid squalane, one of the most important processes

**TABLE 7: Average Values of the Product Translational Energy, $\langle E_T \rangle$, and the Final Scattering Angle, $\langle \theta_f \rangle$, for Representative Reaction Channels as a Function of Incident Angles[a]**

| | | 30° | 45° | 60° |
|---|---|---|---|---|
| | | Inelastic Scattering | | |
| $\langle E_T \rangle$/eV | theory | $0.63 \pm 0.06$ | $1.24 \pm 0.11$ | $1.98 \pm 0.12$ |
| | | $(0.75 \pm 0.11)$ | $(1.48 \pm 0.16)$ | $(2.39 \pm 0.13)$ |
| | expt. | 0.95 | 1.49 | 2.15 |
| $\langle \theta_f \rangle$/° | theory | $38.7 \pm 2.3$ | $46.8 \pm 2.2$ | $53.2 \pm 2.0$ |
| | | $(37.3 \pm 4.2)$ | $(52.3 \pm 3.2)$ | $(57.9 \pm 2.1)$ |
| | expt. | 35.9 | 45.4 | 50.4 |
| | | H Abstraction | | |
| $\langle E_T \rangle$/eV | theory | $0.74 \pm 0.06$ | $1.03 \pm 0.07$ | $1.30 \pm 0.09$ |
| | | $(0.84 \pm 0.10)$ | $(1.41 \pm 0.14)$ | $(1.76 \pm 0.13)$ |
| | expt. | 1.02 | 1.40 | 1.97 |
| $\langle \theta_f \rangle$/° | theory | $38.1 \pm 1.6$ | $40.1 \pm 1.4$ | $45.7 \pm 1.9$ |
| | | $(40.3 \pm 2.5)$ | $(42.8 \pm 2.2)$ | $(49.4 \pm 2.3)$ |
| | expt. | 43.8 | 42.2 | 45.2 |
| | | H Elimination | | |
| $\langle E_T \rangle$/eV | theory | $1.31 \pm 0.09$ | $1.31 \pm 0.08$ | $1.21 \pm 0.07$ |
| $\langle \theta_f \rangle$/° | theory | $40.6 \pm 2.3$ | $40.0 \pm 2.6$ | $38.9 \pm 2.6$ |

[a] The $\theta_f$ is the angle between the velocity vector of the product and the surface normal. The theoretical values in parentheses are generated from products with forward azimuthal angles. The experimental results are obtained from ref 37.

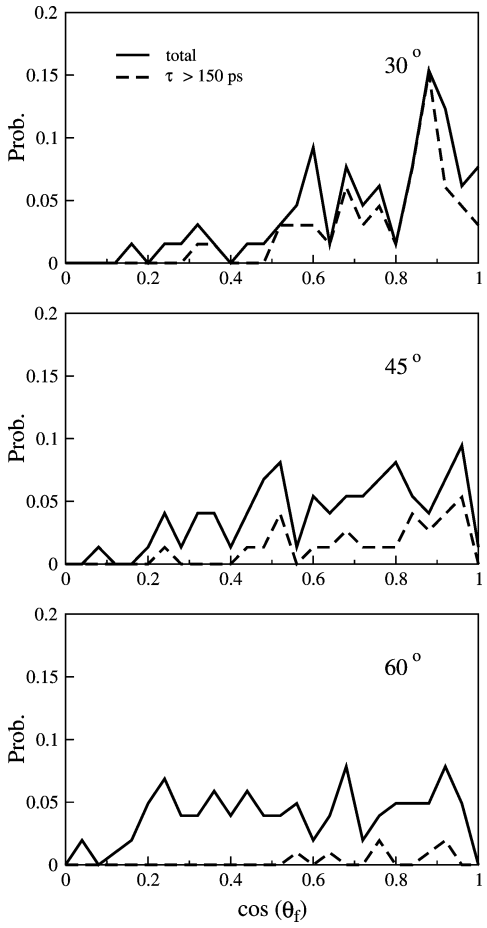


**Figure 6.** Product angular distribution for inelastic scattering at different incident angles.

is inelastic scattering. Figure 6 shows the angular distribution of the exiting O, where $\theta_i$ is the incident angle and $\theta_f$ corresponds to the angle between the surface normal vector and the outgoing velocity vector. To gain insight into how much the two different mechanisms, direct scattering and trapping−desorption, contribute to the angular distribution, the distribution of long-lasting products in the liquid ($\tau$ > 150 fs) is also depicted. Note that all possible azimuthal angles have been included in calculating this angular distribution. The figure shows important variation of the angular distribution with incident angle that reflects the interplay between the trapping−desorption and direct scattering mechanisms. Trapping−desorption is expected to give a cos $\theta_f$ dependence (and therefore a peak at $\theta_f = 0$), while direct scattering should give a peak in the specular direction. At $\theta_i = 60°$, the distribution is quite broad, and the contribution of the long-lasting products is small and concentrated close to the surface normal. Presumably, the absence of a strong specular peak is due to the fact that even the experimentally observed "direct" processes usually involve several encounters due to the surface roughness of liquid squalane such that they can give significant nonspecular scattering. For $\theta_i = 45°$, the distribution is similar to that for $\theta_i = 60°$, but the angular distribution is slightly more concentrated close to the specular angle and surface normal, which is due to the increased contribution of the trapping−desorption mechanism. For $\theta_i = 30°$, the dominant flux escaping from the surface is detected near the surface normal, which is consistent with a more dominant trapping−desorption mechanism. However, it should be noted that a peak from direct scattering is still present.

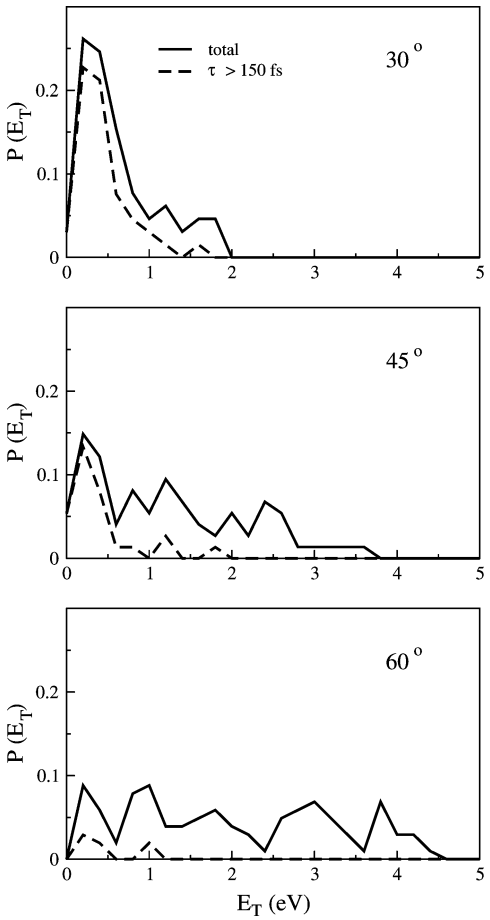


**Figure 7.** Product translational energy distribution for inelastic scattering as a function of the incident angle.

The product translational energy distribution ($E_T$) for inelastic scattering is presented in Figure 7. This shows a broad distribution, with more significant intensity at low translational energies as the incident angle decreases. As a result, the average product translational energy, $\langle E_T \rangle$, which we present in Table 7, shows the same trend. This means that there is greater energy transfer to the liquid for collisions that have a higher

**TABLE 8: Comparison of Simulations of Hyperthermal Inelastic Scattering: $<E_T>$ and $<\theta_f>$**

| | O + SAM[a] | | | |
|---|---|---|---|---|
| | QM/MM | | MD | this work |
| | $\phi = 0°$ | $\phi = 180°$ | $\phi$ random | $\phi$ random |
| $\theta_i = 30°$ | | | | |
| $<E_T>/E_i$[b] | 0.068 | 0.11 | 0.051 | $0.13 \pm 0.01$ |
| $<\theta_f>$ | 22.3 | 27.3 | 39.2 | $38.7 \pm 2.3$ |
| $\theta_i = 45°$ | | | | |
| $<E_T>/E_i$ | 0.11 | 0.23 | 0.11 | $0.25 \pm 0.02$ |
| $<\theta_f>$ | 28.0 | 38.8 | 42.2 | $46.8 \pm 2.2$ |
| $\theta_i = 60°$ | | | | |
| $<E_T>/E_i$ | 0.23 | 0.43 | 0.30 | $0.40 \pm 0.02$ |
| $<\theta_f>$ | 33.8 | 52.5 | 50.9 | $53.2 \pm 2.0$ |

[a] Simulations from Table 10 of ref 21. [b] $E_i$ for the QM/MM and current study is 5 eV, and that for the MD calculation is 5.23 eV. $<\theta_f>$ is in degrees.

normal velocity component, which is a result that connects with our previous picture in terms of greater residence time in the liquid, and a larger number of encounters for smaller incident angles. Indeed, this conclusion is further supported by the results in Table 3, which shows the mean residence time, $<\tau>$. As expected, at an incident angle of 30°, the mean residence time $<\tau>$ is 705 fs, and it decreases to 276 fs at $\theta_i = 45°$ and to 95 fs at $\theta_i = 60°$. In addition, in Figure 3, we see that the collisions lead to a reduction in the final translational energy of the recoiling O. The average number of encounters at 30° (5.4) is indeed larger than that at 45° (3.7) and at 60° (2.7), and the fraction of trajectories with less than five encounters increases with incident angle.

Compared with the earlier O + SAM study,[12,21] energy transfer appears to be relatively inefficient in collisions of O with liquid squalane; see Table 8. This inefficiency is more prominent for the smaller $\theta_i$ where the trapping−desorption process is substantial. This is not particularly surprising since, for the alkane part of the alkanethiol chain, the SAM ($\sim$1.02 g/cm$^3$)[12,38] is approximately 25% denser than squalane ($\sim$0.815 g/cm$^3$), and the SAM has a relatively sharp surface, while squalane has a surface layer of low density with a thickness of around 5 Å. As a result, this relatively low density of squalane will lead to a smaller number of encounters before the O atom can escape.

**C. H Abstraction.** Figure 8 presents angular distributions for the OH radical product. As with inelastic scattering, this distribution becomes more concentrated near the surface normal as the incident angle decreases, where trapping−desorption is increasingly important. This result is also evident in the translational energy distribution (Figure 9), which shows increasing intensity at low energies as the incident angle decreases. We find that, on the whole, trapping−desorption is more important for the abstraction mechanism than for inelastic collisions. Figure 10 shows the relationship between product translational energy and the number of encounters. Here, we see that not only do more collisions induce a larger reduction in the product translational energy but also that the efficiency of energy transfer in the first several collisions depends upon incident angle, although not as strongly as in inelastic scattering. Again, the mean residence time, $<\tau>$, of the product diminishes as the incident angle moves farther from the surface normal (Table 3).

It would be interesting to see how different the correlations of the translational energy versus $N_{enc.}$ are before and after reaction. However, it is not easy to define a reaction point because the transition-state geometry varies depending upon the

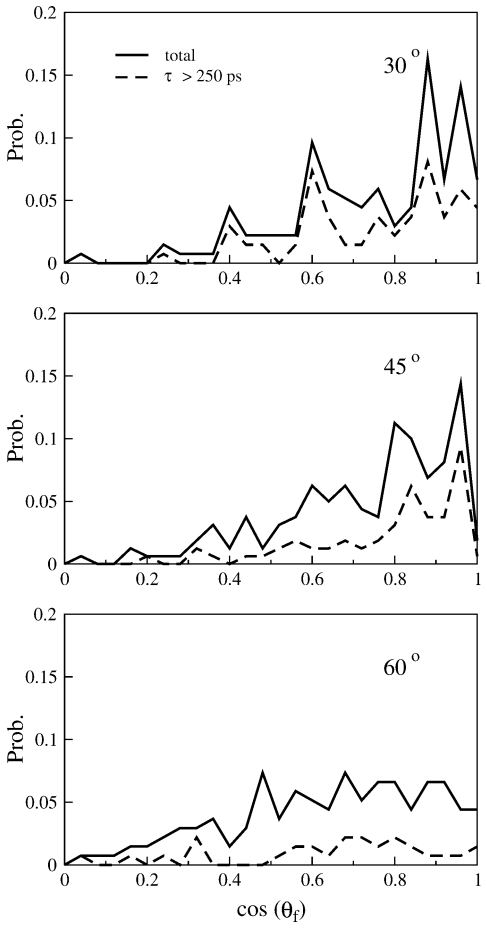


**Figure 8.** Product angular distribution for H abstraction at different incident angles.

identity of the target C−H bond. For technical convenience, we consider only the C−H and O−H bond distances directly involved in the reaction and assume that reaction occurs at the moment when the O−H bond becomes shorter than the C−H bond. The translational energy at that point is then used to determine the change in translational energy before and after reaction, and the resulting distributions of these energies versus the number of encounters is presented in Figure 11. Although the dynamics before and after the reaction occurs is apparently independent of incident angle, we see several dynamics features to note. First of all, reaction dominantly takes place before the incoming O undergoes less than three major encounters. The average number of encounters prior to the reaction is 0.75, 0.66, and 0.74 for 30, 45, and 60° of incidence, respectively. In addition, even when reaction occurs at the first major encounter ($N_{enc.} = 0$), we see substantial energy reduction. While the ignored minor encounters may play a role in this energy decrement, much of the energy loss arises from energy that is used in climbing up the barrier to reaction. No significant dependence of the results on incident angle is found.

On the other hand, we see an energy increment after the reaction in several trajectories where the product undergoes a relatively small number of encounters. This arises from energy released in climbing down the reaction barrier, which, as Troya et al. realized,[6,7] mostly is partitioned into product translational energy. Interestingly, at 30° incidence, this energy increment is negligible compared to that at 45 and 60°, indicating that the efficiency of energy transfer in the first several collisions after reaction depends upon the incident angle. Therefore, the different efficiency of energy transfer stems from dynamics associated with the product OH rather than the reactant O. However, this

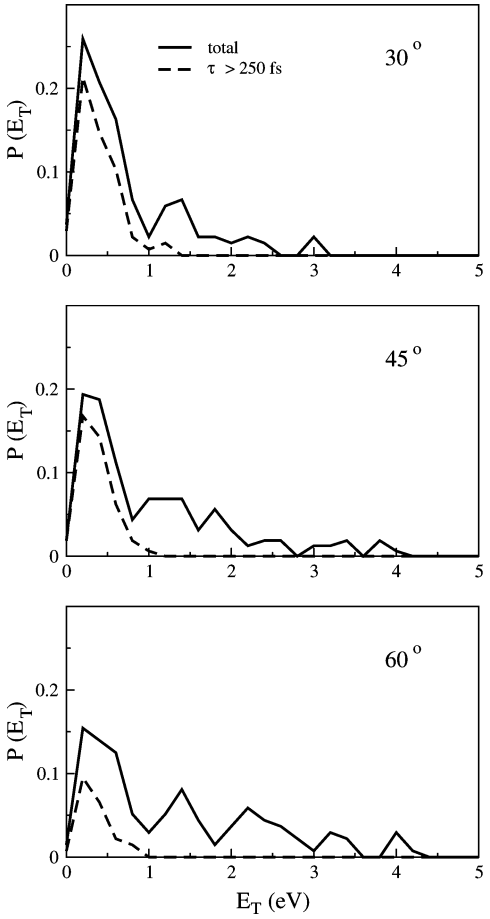


**Figure 9.** Product translational energy distribution for H abstraction as a function of the incident angle.

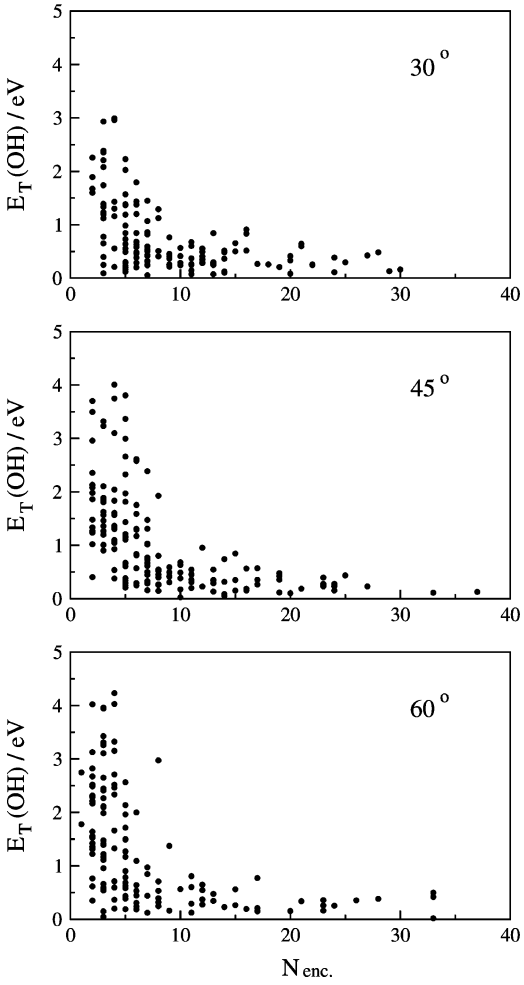


**Figure 10.** Scatter plots of $E_T$ versus $N_{enc.}$ for H abstraction at different incident angles.

feature is not apparent for 45 and 60°, and thus, this seemingly leads to less efficient energy transfer depending upon the incident angle for H abstraction than that for inelastic scattering. We also see a difference in the distribution of a number of encounters after the reaction, which shifts to smaller numbers of collisions as the incident angle increases.

We have also investigated the rotational and vibrational distributions associated with the product OH radical. The quasiclassical histogram method is used to determine these distributions wherein the rotational and vibrational actions are rounded to the nearest integer to define quantum states. Here, we note that in past (SAM) work, it has been demonstrated that rotationally cold products arise via trapping−desorption, whereas hot products arise from direct scattering.[12,19] This trend is also observed in the present study; see Figure 12. For smaller incident angles, the population of rotationally cold OH is more important, which is indicative of rotational relaxation associated with impacts after the OH is produced.[12] The population of low $J_{OH}$, however, is not as substantial as that found in O + SAM collisions at the same energy. This is consistent with the less efficient energy transfer that we noted earlier for inelastic scattering. Direct comparisons of the present results with experiment cannot be made, as the McKendrick work refers to lower collision energies where rotational excitation is lower, while the Minton experiments have not determined rotational excitation information so far. However, one point of caution that we note is that MSINDO is likely to overestimate rotational excitation (as the enthalpies of reaction are overpredicted); therefore, comparisons of these results with experiment will likely find that the calculated rotational excitation is too high.[6,7]

The OH vibrational distribution is best characterized in terms of the ratio $P(\nu' = 1)/P(\nu' = 0)$, as excitation above $\nu' = 1$ is minor. We find that this ratio is approximately 0.13 in our results, which is slightly higher than that for the experiments (for lower collision energy)[17,18] and also higher than earlier estimates for the O + SAM system.[12,19] The ratio is 0.07, 0.11, and 0.26 for abstraction at primary, secondary, and tertiary, respectively. This clearly shows that abstraction of tertiary hydrogen is the main source of the high vibrational excitation. Considering only primary and secondary hydrogens drops the ratio to 0.10, which is in good accord with the previous theoretical studies for the SAM system where there are no tertiary hydrogens.

We note that zero-point energy is not included in the reactants in our simulation. Doing so would likely lead to nonphysical behavior as the squalanes would end up with nonphysically high temperatures after rapid intramolecular vibrational redistribution, and this would lead to evaporation or even dissociation of the molecules. Indeed, Lu and Hase pointed out that there is no fundamental way to choose the fraction of zero-point energy to add to each normal mode of the reactant to make the classical simulation describe quantum dynamics more accurately.[39] Fortunately, these technical deficiencies can probably be ignored at the high energy associated with LEO conditions.[6,7] A more important issue to the accuracy of the vibrational/rotational distributions is the likely overestimation of the reaction exoergicity due to flaws in the MSINDO energetics that we noted earlier.

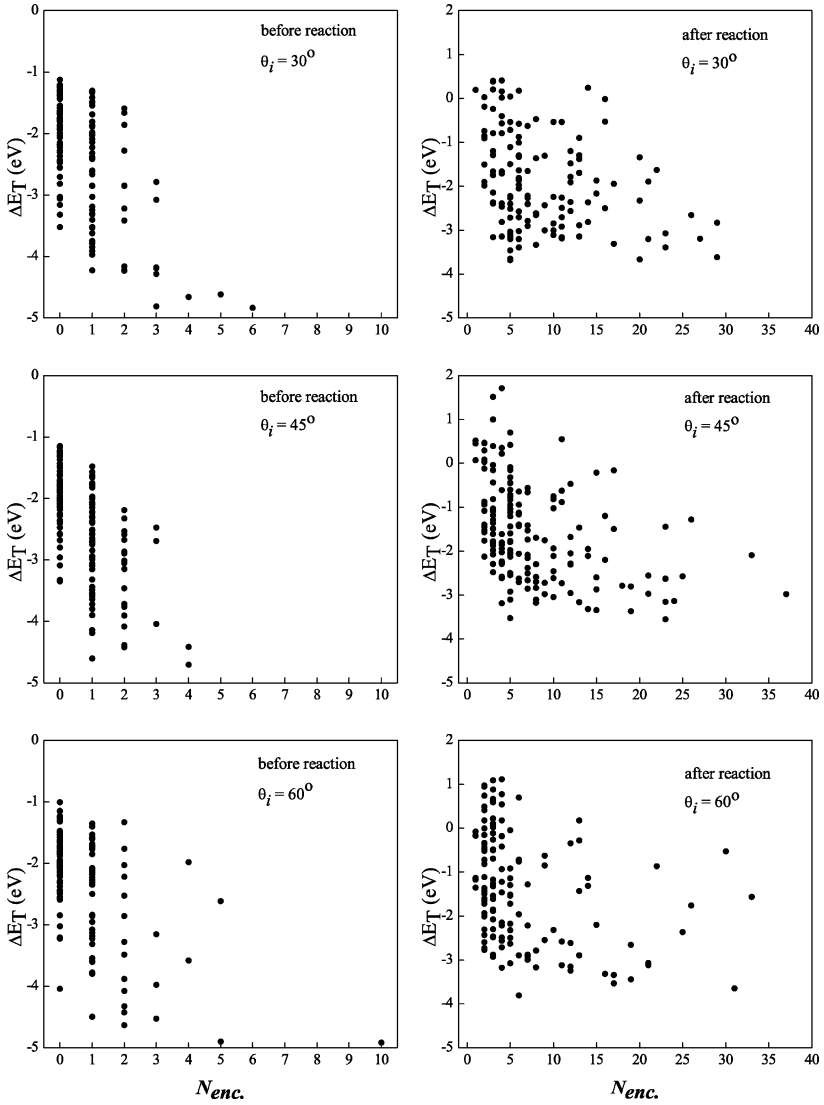


**Figure 11.** Scatter plots of $\Delta E_T$ before (left column) and after reaction (right column) versus $N_{enc.}$ for H abstraction at different incident angles. For the left column, $\Delta E_T$ is defined as $E_T^{rxn} - E_T^0$ (=5 eV), and for the right column, it is $E_T^{final} - E_T^{rxn}$.

**D. H Elimination.** Recently, Minton et al. attempted to detect the eliminated H atom in studies of O + squalane.[11] Unfortunately, however, the hydrogens that they observed seemingly resulted from some other process, such as secondary dissociation of OH/$H_2O$, and they could not obtain meaningful data for H elimination due to the low detection sensitivity of H and the high level of noise.

On the other hand, earlier theoretical calculations[12] agree with our conclusion that H elimination is one of the important reactive processes for hyperthermal collision energies. Table 7 lists the average product translational energy and the average final angle for H elimination. Unlike the other reactive processes, these values do not show significant incident angle dependence. As previously mentioned, the H atoms are eliminated within the first several collisions before the incoming O loses a significant amount of energy and memory of the initial conditions. In addition, once the O atom impinges on a carbon segment, there are several hydrogens eligible for elimination (except for tertiary carbons), and this might contribute to the randomized angular distribution.

**E. C−C Bond Cleavage.** Figure 13 depicts the distribution of the number of carbons contained in the product alkyl or alkoxy radical/ketone along with the corresponding reaction probabilities. The distribution of reaction products of C−C bond cleavage shows that the products are composed mostly of methyl or methoxy radicals and their counterparts having 29 carbons, which is in accordance with experimental observation.[11] $CH_2O$ produced via $CH_3O$ dissociation or double C−C bond scission is also observed and is included in the methoxy radical count. C−C bond cleavage adjacent to a tertiary carbon (−$CH_x$−CH−,

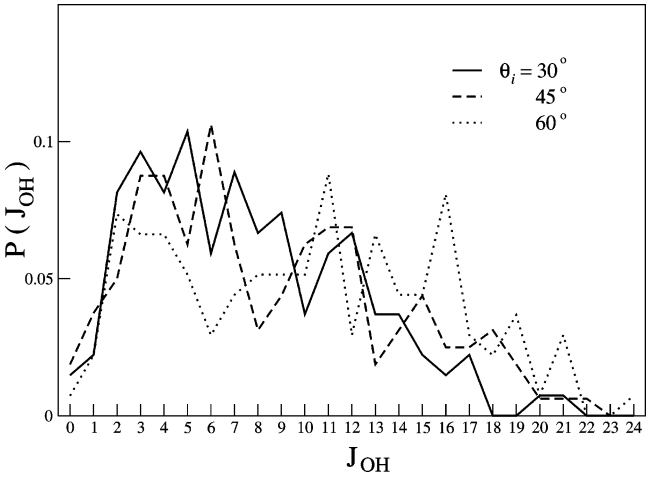


**Figure 12.** OH rotational state distribution.

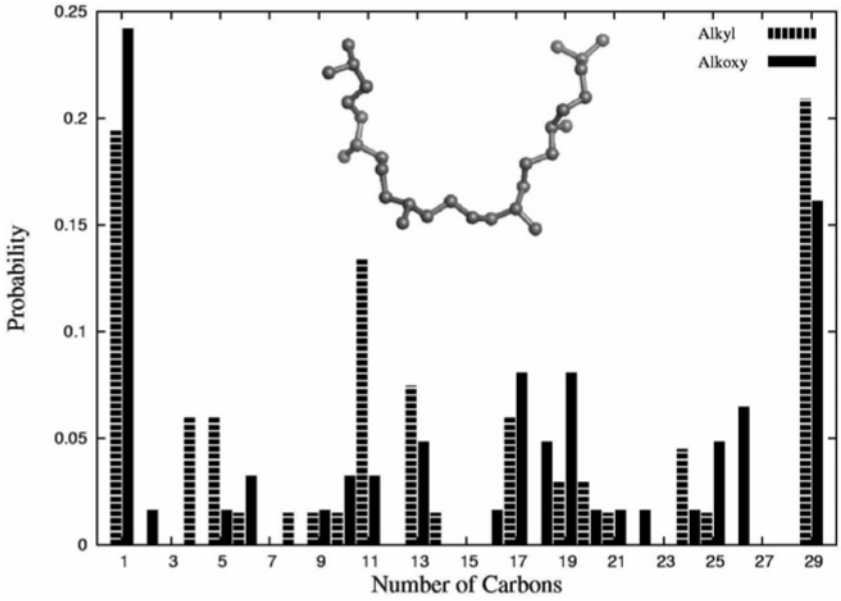


**Figure 13.** Distribution of alkyl and alkoxy/ketone fragments arising from C−C bond cleavage as function of the number of carbons in the fragment. The discrete bar is for the produced alkyl, and the filled bar is for alkoxy/ketone fragments. A single squalane molecule without H atoms is also depicted inside.

where $x = 1$ or 2) is the most prominent process (77.3%) despite the steric hindrance for reaction with a tertiary carbon, producing alkyl, alkoxy, and ketone fragments with 1, 6, 8, 11, 13, 17, 19, 22, 24, and 29 carbons. We assume that this is a consequence of the interplay between the steric hindrance and the relative abundance of C−C bonds. For example, C−C bond breakage is less likely at a primary site than at a tertiary site due to the smaller number of available C−C bonds, even though collisions are more likely with primary sites.

The average kinetic energies of $CH_3O$ and $CH_3$ exiting from the surface are 1.42 and 1.48 eV, respectively, and the average internal energies are 1.56 and 0.26 eV, respectively, which shows that the fragment that contains the incoming O always has the higher internal energy. This is consistent with previous studies.[5−8,14]

Recent experiments by Minton and co-workers[11] show that $CH_3O$ and $CH_2O$ are produced in O + squalane collisions. They observed both hyperthermal and thermal species, implying that they are ejected from the surface via both direct and trapping−desorption mechanisms. We found a few thermal methyl or methoxy radicals, but considering that we truncated our simulations at 3−6 ps and found trapped species more often than in the gas, it is likely that some of the trapped $CH_3O$ species will contribute to the thermalized desorbed population in a longer simulation. Secondary dissociation of $CH_3O$ in the gas phase is also seen in extended simulations for several randomly chosen $CH_3O$ molecules. However, dissociation of trapped species is not found in our limited time simulations.

If 5 eV from the incoming O were distributed among all of the degrees of freedom of the squalane molecules in the active region, the temperature rise would be small (roughly 10 K). A more significant rise (300 K) occurs if 5 eV is distributed to a single squalane molecule. Interestingly, Minton and co-workers report the evaporation of squalane induced by impact of the projectile with the surface. The evaporated squalane molecules are attributed to the elevated local temperature such that the signals of alkyl/alkoxy radicals other than the $CH_3O$-related species become undetectable. While the squalane slabs remained stable even for 3 ps trajectories in the absence of the oxygen, evaporation of squalane occurred frequently in our hyperthermal

**Figure 14.** Snapshot of the squalane slab with a generated OH radical and evaporating squalane molecules after 3.1 ps.

O-atom collisions. As seen in Figure 14, it is even possible that two squalane molecules are evaporated.

While the second and third carbons beneath the surface are not very accessible to the incoming O in the O + alkanethiol SAM chain calculations,[12] alkyl and alkoxy fragments bigger than $CH_3$ or $CH_3O$ can be generated by C−C bond cleavage in reactions between hyperthermal O and liquid squalane that occur well beneath the surface. This is presumably not only due to the relatively low density of squalane but also because the arbitrarily oriented hydrocarbon backbone is more accessible (less shielded by the end methyls). Indeed, we find that alkyl/alkoxy fragments with more than 10 carbon atoms are scattered into vacuum, and occasionally, both fragments that are produced in a reaction are able to exit from the surface. Taking into account that the evaporation of an intact squalane molecule can be induced by collision with the hyperthermal incoming O

(5 eV), it is not surprising that two carbon-containing reactive fragments can scatter from the surface. Nevertheless, the longer fragments are more probable to remain in the liquid phase, and if the high-molecular-weight fragment escapes in a direct process, its kinetic energy is low.

## IV. Conclusion

We have investigated hyperthermal gas−liquid reactions by employing QM/MM hybrid direct dynamics calculations. The results yield similar reaction dynamics features to those of the previous O + SAM studies of inelastic scattering and H abstraction concerning the incident angle dependence of the probability for inelastic and reactive channels, for the relative importance of direct or trapping−desorption mechanisms, and so forth. On the other hand, there are several distinct features of the reaction in squalane. The overall energy transfer in liquid squalane, for instance, is less efficient than that in the SAM system. We correlated this with the relative density of the squalane and SAM systems, as this plays an important role in determining the length of time that the oxygen atom, or nascent products, are trapped beneath the surface. This difference shows up in a variety of product attributes, such as in the distribution of rotational states of the product OH.

C−C bond scission, through which the erosion of polymeric materials in LEO takes place, is found to be slightly more probable in liquid squalane than in the SAM. Despite the steric hindrance, preference for C−C bond breakage at tertiary carbons is significant. Although the major products of C−C bond breakage are $CH_3$, $CH_3O$, and their $C_{29}$ counterparts, reaction also occurs at other locations. All of these findings can be understood based on the tendency for penetration of the projectile, the statistical structural features of the liquid, and the relative barriers for reaction at primary, secondary, and tertiary sites. Hyperthermal energy of the incoming O (5 eV) also turns out to be sufficient to evaporate a couple of squalane molecules.

**Acknowledgment.** This research was supported by AFOSR MURI Grant No. F49620-01-1-0335 and AFOSR Grant FA9550-07-1-0095. The authors wish to thank Timothy K. Minton (Montana State) for helpful discussions.

## References and Notes

(1) Jursa, A. *U.S. Standard Atmosphere*; U.S. Government Printing Office; Washington, DC, 1976.
(2) Murad, E. *J. Spacecr. Rockets* **1996**, *33*, 131.
(3) Leger, L. J.; Visentine, J. T. *J. Spacecr. Rockets* **1986**, *23*, 505.
(4) Minton, T. K.; Garton, D. J. Dynamics of Atomic-Oxygen-Induced Polymer Degradation in Low Earth Orbit. In *Advanced Series in Physical Chemistry: Chemical Dynamics in Extreme Environments*; Dressler, R. Ed.; World Scientific; Singapore, 2001, p 420.
(5) Garton, D. J.; Minton, T. K.; Troya, D.; Pascual, R. Z.; Schatz, G. C. *J. Phys. Chem. A* **2003**, *107*, 4583.
(6) Troya, D.; Pascual, R. Z.; Garton, D. J.; Minton, T. K.; Schatz, G. C. *J. Phys. Chem. A* **2003**, *107*, 7161.
(7) Troya, D.; Pascual, R. Z.; Schatz, G. C. *J. Phys. Chem. A* **2003**, *107*, 10497.
(8) (a) Yan, T.; Doubleday, C.; Hase, W. L. *J. Phys. Chem. A* **2004**, *108*, 9863. (b) Yan, T.; Hase, W. L.; Doubleday, C. *J. Chem. Phys.* **2004**, *120*, 9253.
(9) (a) Garton, D. J.; Minton, T. K.; Alagia, M.; Balucani, N.; Casavecchia, P.; Volpi, G. G. *J. Chem. Phys.* **2000**, *112*, 5975. (b) Garton, D. J.; Minton, T. K.; Alagia, M.; Balucani, N.; Casavecchia, P.; Volpi, G. G. *J. Chem. Phys.* **2001**, *114*, 5958.
(10) Zhang, J.; Garton, D. J.; Minton, T. K. *J. Chem. Phys.* **2002**, *117*, 6239.
(11) Zhang, J.; Upadhyaya, H. P.; Brunsvold, A. L.; Minton, T. K. *J. Phys. Chem. B* **2006**, *110*, 12500.
(12) Diego, T.; Schatz, G. C. *J. Chem. Phys.* **2004**, *120*, 7696.
(13) Jacobs, D. C. *Annu. Rev. Phys. Chem.* **2002**, *53*, 379.
(14) Diego, T.; Schatz, G. C. *Int. Rev. Phys. Chem.* **2004**, *23*, 341.
(15) (a) Nathanson, G. M.; Davidovits, P.; Worsnop, D. R.; Kolb, C. E. *J. Phys. Chem.* **1996**, *100*, 13007. (b) Nathanson, G. M. *Annu. Rev. Phys. Chem.* **2004**, *55*, 231.
(16) (a) Saecker, M. E.; Govoni, S. T.; Kowalski, D. V.; King, M. E.; Nathanson, G. M. *Science* **1991**, *252*, 1421. (b) Saecker, M. E.; Nathanson, G. M. *J. Chem. Phys.* **1993**, *99*, 7056.
(17) (a) Kelso, H.; Köhler, S. P. K.; Henderson, D. A.; McKendrick, K. G. *J. Chem. Phys.* **2003**, *119*, 9985. (b) Köhler, S. P. K.; Allan, M.; Kelso, H.; Henderson, D. A.; McKendrick, K. G. *J. Chem. Phys.* **2005**, *122*, 024712.
(18) Köhler, S. P. K.; Allan, M.; Costen, M. L.; McKendrick, K. G. *J. Phys. Chem. B* **2006**, *110*, 2771.
(19) Li, G.; Bosio, S. B. M.; Hase, W. L. *J. Mol. Struct.* **2000**, *556*, 43.
(20) Köhler, S. P. K.; Reed, S. K.; Westacott, R. E.; McKendrick, K. G. *J. Phys. Chem. B* **2006**, *110*, 11717.
(21) Tasić, U. S.; Yan, T.; Hase, W. L. *J. Phys. Chem. B* **2006**, *100*, 11863.
(22) Mondello, M.; Grest, G. S. *J. Chem. Phys.* **1995**, *103*, 7156.
(23) (a) Gao, J.; Luedtke, W. D.; Landman, U. *J. Chem. Phys.* **1997**, *106*, 4309. (b) Gao, J.; Luedtke, W. D.; Landman, U. *J. Phys. Chem. B* **1997**, *101*, 4013.
(24) Gupta, S. A.; Cochran, H. D.; Cummings, P. T. *J. Chem. Phys.* **1997**, *107*, 10316.
(25) Balasubramanian, S.; Klein, M. L.; Siepmann, J. I. *J. Phys. Chem.* **1996**, *100*, 11960.
(26) Wick, C. D.; Siepmann, J. I.; Schure, M. R. *Anal. Chem.* **2002**, *74*, 3518.
(27) Allinger, N. L.; Yuh, Y. H.; Lii, J.-H. *J. Am. Chem. Soc.* **1989**, *111*, 8551.
(28) Jorgensen, W. L.; Maxwell, D. S.; Tirado-Rives, J. *J. Am. Chem. Soc.* **1996**, *118*, 11225.
(29) Ponder, W. A.; Richards, F. M. *J. Comput. Chem.* **1987**, *8*, 1016.
(30) Bakowies, D.; Thiel, W. *J. Phys. Chem.* **1996**, *100*, 10580.
(31) (a) Ahlswede, B.; Jug, K. *J. Comput. Chem.* **1999**, *20*, 572. (b) Jug, K.; Geudtner, G.; Homann, T. *J. Comput. Chem.* **2000**, *21*, 974. (c) Bredow, T.; Geudtner, G.; Jug, K. *J. Comput. Chem.* **2001**, *22*, 89.
(32) Kerdcharoen, T.; Liedl, K. R.; Rode, B. M. *Chem. Phys.* **1996**, *211*, 313.
(33) Kerdcharoen, T.; Morokuma, K. *Chem. Phys. Lett.* **2002**, *355*, 257.
(34) Heyden, A.; Lin, H.; Truhlar, D. G. *J. Phys. Chem. B* **2007**, *111*, 2231.
(35) Troya, D.; Schatz, G. C.; Garton, D. J.; Brunsvold, A. L.; Minton, T. K. *J. Chem. Phys.* **2004**, *120*, 731.
(36) Bolton, K.; Svanberg, M.; Petterson, J. B. C. *J. Chem. Phys.* **1999**, *110*, 5380.
(37) Minton, T. K. Montana State University: Bozeman, MT, 2006; Personal communication.
(38) Schreiber, F. *Prog. Surf. Sci.* **2000**, *65*, 151.
(39) Lu, D.; Hase, W. L. *J. Chem. Phys.* **1989**, *91*, 7490.